

Ion-mediated charge-charge interactions drive aggregation of surface-functionalized gold nanoparticles

Emanuele Petretto¹, Quy K. Ong², Francesca Olgiati², Mao Ting², Pablo Campomanes¹, Francesco Stellacci² and Stefano Vanni^{1}*

1. Department of Biology, University of Fribourg, Chemin du Musée 10, 1700 Fribourg, Switzerland

2. Institute of Materials, Ecole Polytechnique Federale de Lausanne, 1015 Lausanne, Switzerland

KEYWORDS Nanoparticles; colloidal stability; hydrophobic interactions; aggregation; Cryo-EM; molecular dynamics,

ABSTRACT

Monolayer-protected metal nanoparticles (NPs) are not only promising materials with a wide range of potential industrial and biological applications, but they are also a powerful tool to investigate the behavior of matter at nanoscopic scales, including the stability of dispersions and colloidal systems. This stability is dependent on a delicate balance between electrostatic

and steric interactions that occur in the solution, and it is described in quantitative terms by the classic Derjaguin-Landau-Verwey-Overbeek (DLVO) theory, that posits that aggregation between NPs is driven by hydrophobic interactions and opposed by electrostatic interactions. To investigate the limits of this theory at the nanoscale, where the continuum assumptions required by the DLVO theory break down, here we investigate NP dimerization by computing the Potential of Mean Force (PMF) of this process using fully atomistic MD simulations. Serendipitously, we find that electrostatic interactions can lead to the formation of metastable NP dimers. These dimers are stabilized by complexes formed by negatively charged ligands belonging to distinct NPs that are bridged by positively charged ions present in solution. We validate our findings by collecting tomographic EM images of NPs in solution and by quantifying their radial distribution function, that shows a marked peak at interparticle distance comparable with that of MD simulations. Taken together, our results suggest that not only hydrophobic interactions, but also electrostatic interactions, contribute to attraction between nano-sized charged objects at very short length scales.

INTRODUCTION

The stability of dispersions and colloidal systems is an important requirement in biological environments as well as in the formulation of industrial products, including in manufacturing, food, and pharma. This stability is dependent on a delicate balance between the electrostatic and steric interactions that occur in the solution, and it is described in quantitative terms by the classic Derjaguin-Landau-Verwey-Overbeek (DLVO) theory¹.

The DLVO theory is generally adequate for large particles or in the long-range regime, but at smaller (“nano”) length scales, the continuum assumptions required by the DLVO theory break down. As a consequence, several discrepancies arise between the DLVO predictions and experimental results, due to deficiencies in the appropriate description of solvent polarization², finite size of ions³, and hydration forces^{4,5}. These discrepancies, generally defined as non-

DLVO forces, can lead to unreliable predictions when the interparticle distance is less than 2 nm¹.

Self-assembled monolayer-protected nanoparticles (SAM-NPs) have emerged in the last few years as a powerful tool to investigate non-DLVO forces⁶⁻⁸. In addition to their extremely promising application potential in a variety of fields, including biology⁹, biomedicine¹⁰, sensing¹¹, and catalysis¹², the chemistry of SAM-NPs makes them particularly well-suited to investigate aggregation propensity and dispersion stability of NPs in solution.

SAM-NPs are nanomaterials consisting of a metal core coated with a ligand shell. This shell, composed by thiolate ligands^{9,13-15} such as alkanethiols¹⁶, oligonucleotides¹⁷, or polyethylene glycols¹⁸, defines the boundaries between the NPs and the surrounding environment, and it provides the NP with both colloidal stability and specific functionality. As a consequence, the physicochemical properties of NPs can be tailored by changing the functional groups, allowing to design advanced materials able to exert specific functions¹⁹. However, even though this class of material is technologically highly meaningful, we still lack a consensus quantitative understanding of how surface chemistry, and namely hydrophobicity and charge localization, might influence the aggregation energy.

In fact, as a result of their nanometer scales, NPs are characterized by an extremely high surface-to-volume ratio and, therefore, NPs in solution tend to aggregate in order to minimize the surface energy, resulting in the rapid settling of the suspension¹. Numerous previous studies have focused on the role of charges²⁰, solvent ion concentration²¹, solubility, and wettability²², and it has been demonstrated that the charge and morphology of the ligand shell play a fundamental role on determining NPs' properties²³.

In this context, computer simulations have emerged as a promising approach to evaluate the interactions between NPs as well as the underlying molecular details²⁴⁻²⁹. For example, Monte Carlo simulations demonstrated that ligand-mediated short-range attractive interactions

between monolayer-protected AuNPs can lead to aggregation despite long-range electrostatic energy barriers²⁹. All-atom Molecular Dynamics (MD) emphasized that the aggregation energy profile between polyethylene coated gold NPs is driven by short-range attraction and characterized by a large attractive well²⁵, while coarse grained model demonstrated the effect of surface chemistry and coverage on the aggregation of thiol coated AuNPs²⁸. Taken together these studies confirmed that hydrophobic interactions are the driving force behind NP aggregation, in agreement with the DLVO framework.

In this work, we investigate NP aggregation as a function of ligand shell chemistry by computing the Potential of Mean Force (PMF) of this process using fully atomistic MD simulations. Unlike previous reports, we find that charge-charge interactions lead to the formation of metastable NP dimers. These dimers are stabilized by complexes formed by negatively charged ligands of the two NPs and positively charged ions. We validate our findings by collecting tomographic EM images of NPs in solution and by quantifying their radial distribution function, that shows a marked peak at an interparticle distance comparable with that of MD simulations. Taken together, our results suggest that not only Van der Waals forces, but also electrostatic interactions, contribute to attraction between nano-sized charged particles at very short length scales.

RESULTS

Potential of Mean Force between highly charged NPs reveals the presence of a non-DLVO metastable minimum. In order to understand the role of the ligand shell composition on the free energy of aggregation, we estimated the potential of mean force (PMF) between identical NPs using umbrella sampling simulations (see Materials and Methods for details). We used three different coatings for the model NPs: 100%OT, random 50%OT:50%MUA (“50%OT”) and random 33%OT:67%MUA (“33%OT”). For purely hydrophobic NPs (100%OT), the PMF

shows that there is no interaction between the two NPs until the distance between their center of mass (interparticle distance) is ~ 3.5 nm; at shorter distances, they start attracting each other (Figure 1A). Interestingly, this distance is about twice the length, measured from the NP surface, of an OT ligand in its most extended state (Supplementary Information, Figure S1). Moreover, according to the computed PMF, the aggregation of 100%OT NPs is a barrierless process leading to a primary minimum that is $59.2 \text{ kcal mol}^{-1}$ more stable than the fully separated state. This indicates that this primary minimum corresponds to a highly stable aggregated state, in agreement with experimental observations²².

For mixed NPs (50%OT and 33%OT), we observed two major differences with respect to the purely hydrophobic 100%OT NPs. First, the stability of the primary minimum with respect to the fully separated state is smaller in the presence of charged ligands, being of 42.3 and $38.3 \text{ kcal mol}^{-1}$, respectively, for the 50%OT and the 33%OT (Figure 1A). Second, NPs aggregation is not spontaneous anymore, and there is an energy barrier, due to the presence of negative charges on the NP surface, that must be overcome to reach the aggregated state. This “electrostatic” energy barrier for aggregation appears at an interparticle distance $\zeta \sim 3.5$ nm and amounts to 4.4 and $8.7 \text{ kcal mol}^{-1}$ for the 50%OT and 33%OT NPs, respectively (Figure 1A). Taken together, our results quantify to what extent the ligand shell composition plays a role in determining the aggregation energy, and they are consistent with predictions based on DLVO theory, namely that aggregation between NPs is driven by hydrophobic interactions and opposed by electrostatic interactions^{30,31}.

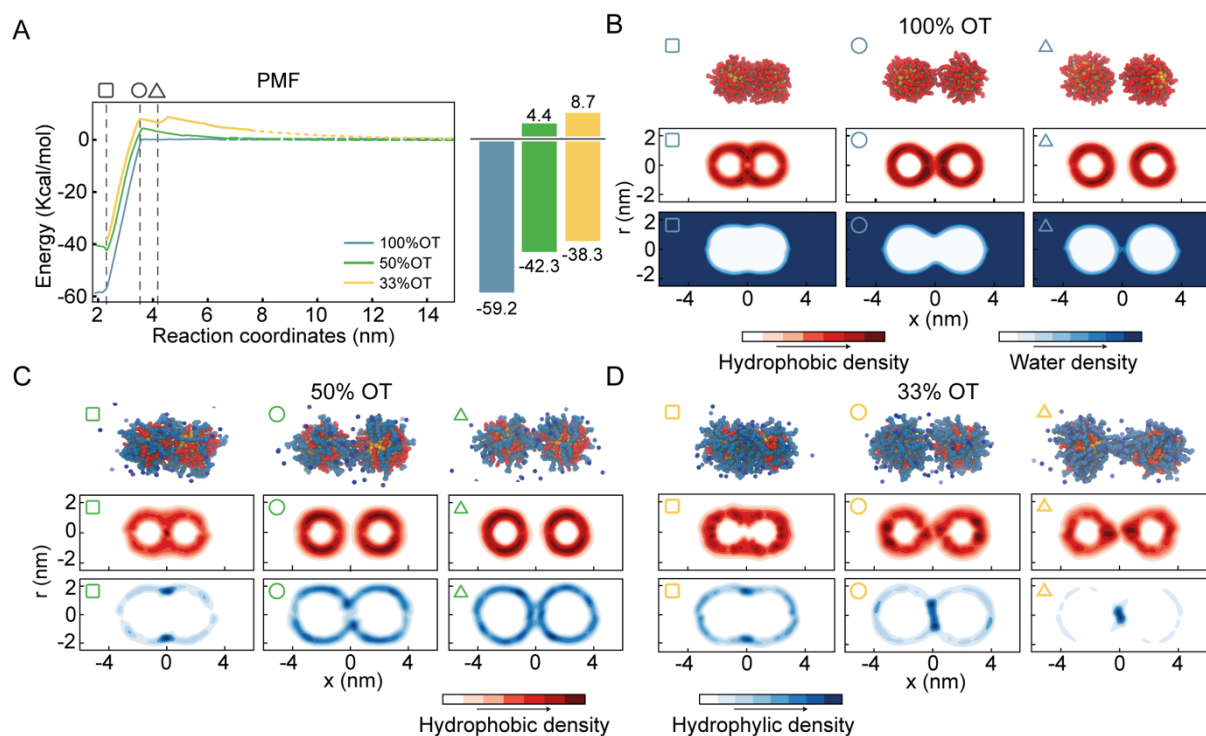


Figure 1: Aggregation behavior of surface-functionalized (MUA-OT) gold nanoparticles (NPs). (A) Dimerization potentials of mean force (PMFs) between identical NPs. Light blue: 100%OT; Green 50%OT; yellow: 33%OT. (B) Density maps for 100%OT NPs at different interparticle distances (square: 2.2 nm, circle: 3.5 nm, triangle: 4.2 nm). Top: snapshot of the interacting dimer; Middle: hydrophobic density; Bottom: water density. (C) 50%OT and (D) 33%OT ligand density maps as function of interparticle distance. Top: snapshot of the interacting dimer; Middle: hydrophobic density; Bottom: hydrophilic density.

Quite unexpectedly, however, we observed the presence of a secondary minimum in the energy profile for the 33%OT NP (Figure 1A, yellow curve). To further investigate this observation, we first analyzed the dimers' geometrical properties. To this end, we calculated separately the density of both the hydrophobic and hydrophilic beads as a function of the interparticle distance. Figure 1B shows the density maps for the hydrophobic atoms (middle panel) and water (bottom panel) in the case of the 100%OT NPs at different interparticle distances. In all the plots, the interparticle distance increases from left to right. At short core-core distances ($\zeta \sim 2.2$ nm), the contact site is completely determined by hydrophobic interactions between the OT ligands, and water molecules are not able to come close to the geometrical center of the dimer (Fig. 1B, left). For intermediate distances ($\zeta \sim 3.5$ nm), the hydrophobic ligands in the 100%OT appear elongated, binding together the dimer (Fig. 1B, center). For larger interparticle distances (ζ

~4.2 nm), water molecules are able to penetrate and approach the dimer interface and physically separate the aliphatic ligands (Fig. 1B, right).

Figures 1C and 1D show the average density for both the aliphatic chains and the charged beads for 50%OT and 33%OT, respectively. For both systems, at the minimum separation distance ($\zeta \sim 2.2$ nm), the contact site is completely hydrophobic (Fig. 1C and 1D, left) and the density profile for the hydrophilic ligands shows an accumulation in the boundaries of the interfacial region in a ring-shaped fashion. At larger distances ($\zeta \sim 3.5$ nm), however, important differences between the 50%OT and the 33%OT NPs can be observed, as the hydrophilic beads in the 50%OT NP do not populate the interfacial region, while for the 33%OT NPs a higher hydrophilic density and a general deformation, from ring shaped to disk shaped, can be observed in the contact region. This difference in behavior becomes even more pronounced at larger distances ($\zeta \sim 4.2$ nm).

Overall, this analysis suggests a correspondence between the ligands' organization at the interface, in particular referring to the hydrophilic beads, and the observed presence of a metastable minimum in the aggregation PMF.

The metastable dimer of highly charged NPs originates from the complexation between charged ligands. From the analysis of the distribution of hydrophilic and hydrophobic ligands among the NPs, it appears that the unexpected presence of a distinct minimum in the PMF of the 33%OT system at 4.2 nm might originate from the interaction between charged ligands. To test this hypothesis, we further investigated the behavior of hydrophilic ligands and counterions along the reaction pathway.

To obtain a better picture on the aggregation pathway for the 33%OT, we explored NP-NP behavior for distinctive core-core distances where we observed sudden changes in the energy profile: (a) at 2.2 nm, the minimum distance of interaction (Fig. 2A, point a, white); (b) at 3.6

nm, the aggregation barrier (Fig. 2A, point b, light gray); (c) at 4.2 nm, the newly found minimum (Fig. 2A, point c, grey); (d) at 4.6 nm, where the NPs are fully separated (Fig. 2A, point d, dark grey). As it can be appreciated in Fig. 2B, as the two NPs separate from each other, ligands extend at the interface between the two NPs and interact not only amongst them, but also with multiple positively charged sodium ions.

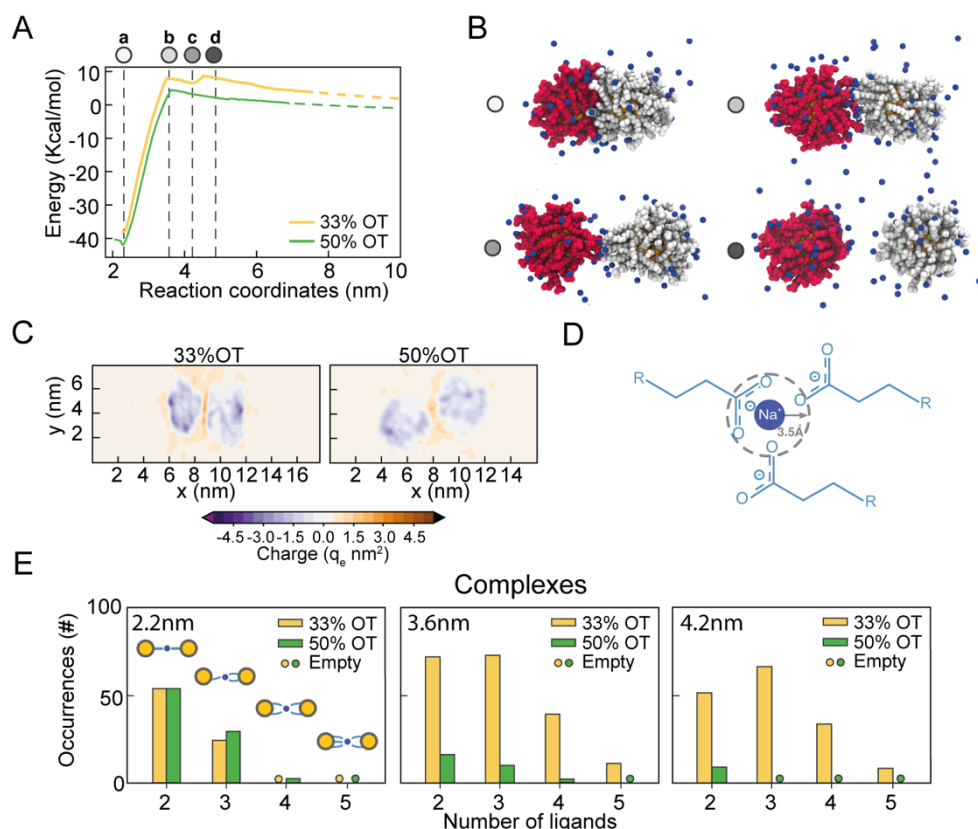


Figure 2: The secondary minimum in the NP-NP PMFs is characterized by ion-mediated interparticle complexes. A. Potential of mean force of dimerization for 33%OT and 55%OT NPs. Selected remarkable points characterizing the energy profile are highlighted: a) first minimum; b) first barrier, c) second local minimum, d) completely separated NPs. B. Snapshots of the highlighted distances in the PMF. Colors are used to visually separate the NPs in the dimer, sodium ions are shown in blue. C. Electrostatic density maps for 33%OT and 50%OT at 4.2 nm interparticle distance. D. Pictorial representation of charged ligand-ion-charged ligand interparticle complexes. E. Occurrences of charged ligand-ion-charged ligand interparticle complexes at different interparticle distances.

To further characterize the role of electrostatic interactions in the aggregation of charged NPs, we first computed the electrostatic density maps for two NPs, 33%OT and 50%OT, at 4.2 nm interparticle distance, *i.e.*, where the newly found minimum was observed for 33%OT but not

for 50%OT (Figure 4C). Quite interestingly, the heat maps show that despite the high negative charge given by the presence of the NPs, the systems have a net positive charge at the interface, and that this charge is higher in the case of 33%OT, further indicating the presence of multiple positive sodium ions at the interface between the two identical NPs.

To better discriminate this behavior at the atomistic level, we next computed the occurrences of $\text{R-COO}^- \cdot \text{Na}^+ \cdot \text{COO-R}$ complexes for both the inter-NPs interactions. We defined the formation of a complex when a sodium ion lies within 0.35 nm of two or more carboxylates simultaneously (Fig. 2D). Remarkably, we observed that moving away from the primary minimum, the two 33%OT NPs engage in multiple 3-mer and 4-mer inter-NP complexes involving multiple charged ligands, while this is instead not the case for the 50%OT NPs (Figure 2E).

Patterning of ligands on the NP surface modulates the appearance of a metastable minimum. Our data suggest that ion-mediated charge-charge interactions between surface ligands promote the appearance of a metastable secondary minimum between highly charged NPs (33%OT), and that this minimum is absent in NPs with lower charge (50%OT). As this phenomenon appears to be driven by the organization of the surface ligands at the interface between NPs, we next wondered whether a reorganization of the ligand shell topography could lead to a similar behavior even in NPs with overall lower total charge.

To test this hypothesis, we designed two new distinct surface patterns for the 50%OT NPs: 1) Completely asymmetrical “Janus-like” NPs, with all OT ligands in one half of the NPs and all MUA ligands on the other side; 2) Striped NPs with MUA patches at the poles and an OT ligands strip located at the equator. We next compared these two new patterns with the fully random 50%OT we previously investigated (Figures 2 and 3), where OT and MUA ligands are

randomly distributed throughout the NP surface (Figure S2). Despite the difference in shell topography, all NPs have the same OT/ MUA ratio (50%OT, 50%MUA) and charge (-30 q_e).

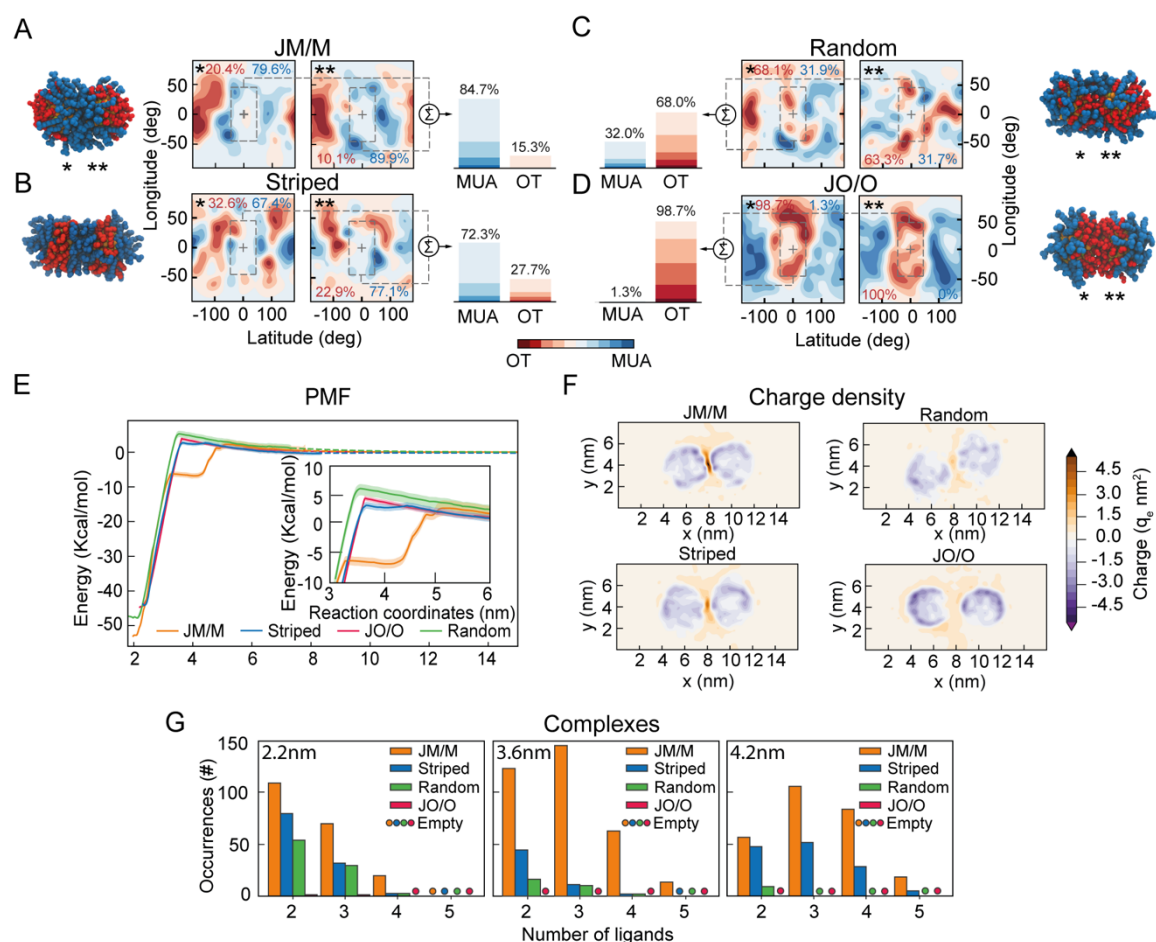


Figure 3: Patterning of ligands on the surface of low-charge NP modulates the appearance of a metastable minimum. A-D. NP-NP dimers for JM/M, Striped, Random, and JO/O conformation. Left: Representative snapshots. OT: red, MUA: blue. Middle: Ligand density maps at the NP-NP interface. Right: effective ligands' coverage percentage. E. Corresponding PMFs; F. Charge density at the NP-NP interface at 4.2 nm interparticle distance. G. Occurrences of charged ligand-ion-charged ligand interparticle complexes at different interparticle distances

Afterward, we prepared dimers of identical NPs, choosing the relative orientation between the NPs to define the number of MUA ligands at the interface. Thus, we arranged the NPs in four different ways: 1) a pair of Janus NPs with the MUA side at the interface (JM/M) (Figure 3A); 2) a pair of striped NPs with the MUA patches at the interface (Figure 3B); 3) a pair of random NPs randomly oriented (Figure 3C); and 4) a pair of Janus NPs with the OT side at the interface (JO/O) (Figure 3D). To quantify the number of charged ligands at the interface for these

orientations, we generated ligand density maps at minimum core-core distance (~ 2.2 nm) (Figure 3A-D). In these maps OT and MUA local densities are represented in red and blue, respectively, while light color means an equiprobability to find both ligands. The dashed lines identify the interface between NPs. From these maps, we quantified the effective ligands' coverage percentage of the interface via a simple sum of the various (OT, red; MUA, blue) contributions (Figure 3A-D). These data confirm that there is a trend in the number of charged ligands at the interface with JM/M ($85 \pm 1\%$) > Striped ($72 \pm 5\%$) > Random ($32 \pm 0.1\%$) > JO/O ($1 \pm 0.7\%$).

Next, to properly quantify the role of the interfacial ligand topography on the free energy of aggregation, we computed the separation PMFs for the aforementioned orientations (Figure 3E). The PMFs show that the primary minimum is located at $\zeta \sim 2.2$ nm for all systems (Figure 3E). As expected, the electrostatic aggregation barrier is similar for all topographies (Figure 3E), as this barrier is modulated by the total charge on the NP according to the classical DLVO theory.

However, both JM/M and Striped arrangements exhibit a secondary metastable minimum in the energy profile, like the one previously observed for the 33%OT NP (Figure 1). For the JM/M NPs, the metastable state is located at values of ζ between 3.5 nm and 4.2 nm, and the energy required to overcome this barrier and fully separate the NPs is ~ 6 kcal. On the other hand, the Striped secondary barrier is shallower (~ 1 kcal) and within the PMF statistical error. Overall, these data suggest that, for a given ratio of hydrophobic vs. charged ligands on the NP shell, the organization of charged ligands on the NP surface modulates the appearance of this metastable state. Increasing the number of charged ligands at the interface, like in JM/M and Striped (Figure 3A-D), correlates with the presence of the metastable state.

To further investigate the molecular properties of this minimum, we next explored the distribution of ions and charged ligands at the interface and around the NPs at an interparticle

distance compatible with the secondary minimum ($\zeta \sim 4.2$ nm). Figure 3F depicts the charge density for the four systems. Consistently with the maps previously computed for the random 33%OT and 50%OT NPs (Figure 2), the heat maps for these four systems show that, as the number of charged ligands at the interface increase, the charge density also increases. Overall, these data further confirm that highly negatively charged patches at the interface might be able to accumulate ions and promote dimer stabilization.

Finally, to further correlate the presence of a secondary minimum with the formation of interparticle charge-ion-charge complexes, we quantified the formation of these complexes as a function of the core-core distance for the various surface patterns (Figure 3G). As expected, their number increases with the number of charged ligands at the interface (Figure 3G). Remarkably, for interparticle distances of 4.2 nm, no or negligible complex formation is observed for the random and JO/O homodimers, while substantial formation of interparticle complexes can be observed at the interface for the JM/M and Striped ones. Of note, these complexes are solely promoted by a rearrangement of the ions towards the NP-NP interface, as the total charge of the two NPs plus their surrounding ions remains constant at all interparticle distances (Figure S3).

NPs in solution form dimers at interparticle distances comparable with those predicted by MD simulations. In order to validate the main observation extracted from the MD simulations (*i.e.* that charged NPs form dimers in solution at interparticle distances of approximately 2 times the radius of the metal core plus the ligand shell) and to assess whether this is a general rule for NP functionalized with a binary self-assembled monolayer of hydrophobic and hydrophilic surfactants, we next prepared two sets of gold nanoparticles that were functionalized with a binary self-assembled monolayer (SAM) of thiols and investigated their dispersion states by cryogenic electron tomography (cryo-ET). The first sample (namely, MUS:OT) was composed of a gold NP core (average diameter of 4.6 nm, Figure S4) functionalized with 11-

mercaptoundecane sulfonate (MUS, 70%) and OT (30%). The other sample was MUA:OT that was made of gold NP core with an average diameter of 3.9 nm (Figure S4) and functionalized with 11-mercaptoundecanoic acid (MUA, 84%) and OT (16%). Here, OT was chosen to mimic the hydrophobic component of the two thiols in the MD simulations, while MUS and MUA function as salt bridging thiolated ligands. The quantification of the interparticle distance between NPs can be achieved by cryogenic electron tomography (cryo-ET) via the radial distribution function (RDF) calculated from the spatial positions of the NPs³². In the cryo-ET approach, an aqueous dispersion of the NPs was vitrified quickly so that the frozen sample maintained the state of the dispersion prior to vitrification. The vitrified sample was subsequently imaged by transmission electron microscopy at cryogenic temperature (-176°C) and at a series of tilt angles. The obtained tilt series was then aligned and further used to reconstruct a tomogram (i.e. 3D image) of the sample. From the tomogram, NPs were identified, and their centroid positions were used to calculate the corresponding RDFs.

Figure 4A and 4B show a representative tomogram of a sample of MUS:OT and of MUA:OT, respectively. From the tomograms, various aggregate states of NPs can be directly visualized. A few of such oligomeric states are represented in Figure 4C-E as a dimer, trimer, and tetramer. RDFs calculated from centroid positions of NPs identified in the tomogram are plotted in Figure 4F for MUS:OT and Figure 4G for MUA:OT sample. The first nearest neighbor distances were clearly determined by the maximum peaks observed in the RDF for both samples. Those can be observed at 6.5 nm and 6.0 nm for MUS:OT and MUA:OT, respectively (Figure 4F,G). These distances are higher than the sum of particle core diameters, that are of 4.6 nm and 3.9 nm, respectively (Figure 4F,G and Figure S4), and the average interparticle distance is about 1.9-2.1 nm larger than the sum of particle core diameters. This value is more than twice the length of the hydrophobic ligand (OT) in its most extended state, suggesting that the NP oligomeric states are mediated by the longer ligands, MUA and MUS, for MUA:OT

and MUS:OT NPs respectively. Also, the observed experimental values of 1.9-2.1 nm are in perfect agreement with the MD simulations, where the ion-mediated minimum between the NPs is found at a distance that is 2.0 nm larger than the core-core minimum distance ($\zeta \sim 4.2$ nm vs $\zeta \sim 2.2$ nm, Figure 1A).

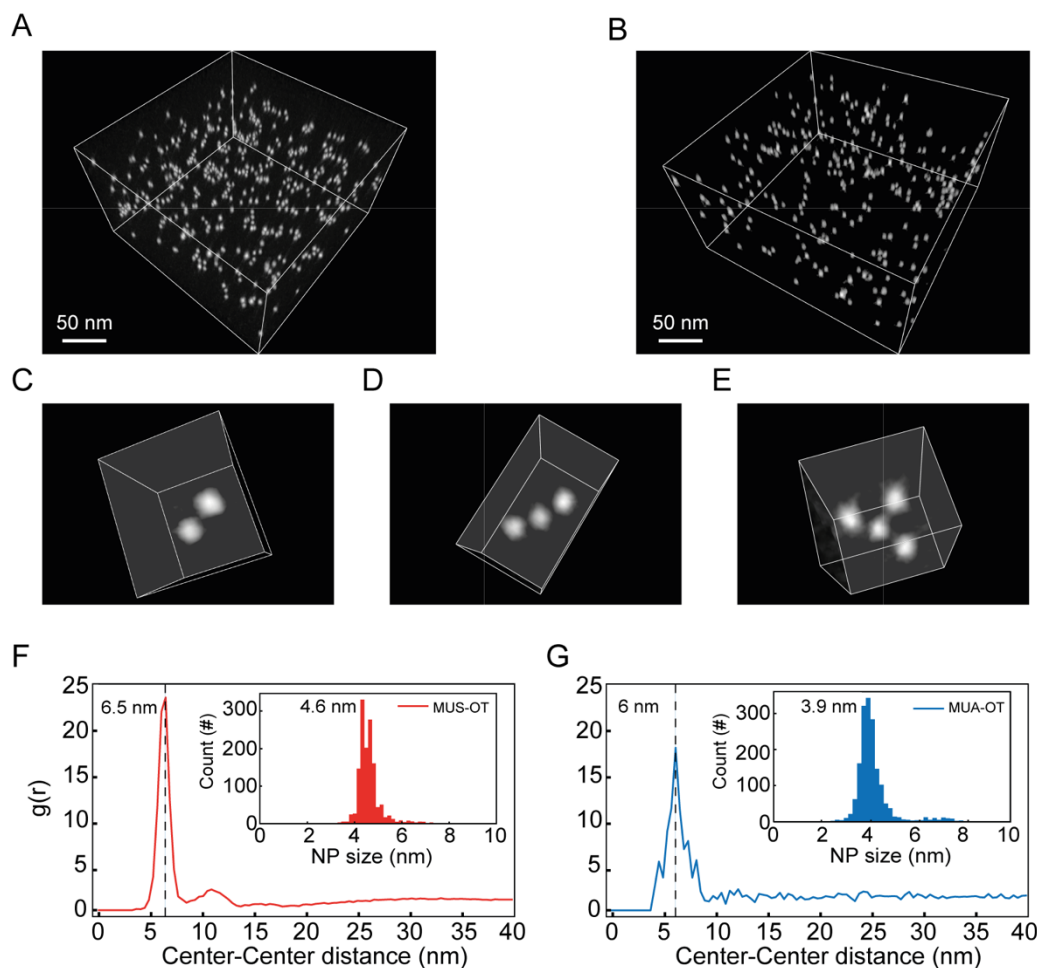


Figure 4: Cryo-ET of vitrified aqueous dispersion of NPs. A. Tomogram of gold NP functionalized with a mixture of MUS (70%):OT (30%) dispersed in water. B. Tomogram of gold NP functionalized with a mixture of MUA (84%):OT (16%) dispersed in NaOH 30mm. C-E. Representative oligomer states found in these sets of samples; C: dimer, D: trimer, E: tetramer. F. Radial distribution function plotted as function of NP-NP centroid distance for MUS:OT sample. The size-distribution of the corresponding NPs is shown in the inset. G. Radial distribution function plotted as function of NP-NP centroid distance for MUA:OT sample. The size-distribution of the corresponding NPs is shown in the inset.

CONCLUSIONS

In this work, we have extensively characterized the dimerization PMFs between identical NPs containing different ratios of hydrophobic/charged ligands and with different ligand patterns

on the NP surface. In agreement with the DLVO theory, we found that the primary minimum describing irreversible NP aggregation is driven by hydrophobic interactions, while the barrier that prevents such aggregation is modulated by the electrostatic repulsion between two NPs of identical charge. We foresee that the extensive quantitative characterization of the dimerization profile of identical NPs we provide here will be useful for the validation and the development of extensively used CG models to describe the behavior of NPs in biological-like contexts^{10,33,34}. Serendipitously, we found that as the charge on the NP surface increases, a metastable minimum along the dimerization PMF appears. Notably, this minimum is found at an interparticle distance that is compatible with fully extended surface ligands barely touching each other. Our analyses suggest that this minimum correlates with the presence of charged ligand-ion-charged ligand complexes, and it is thus of electrostatic origin. Unlike the primary minimum, this minimum is metastable and thus potentially reversible.

In addition, we showed that the presence of this metastable state can be modulated by the patterning of ligands on the NP surface. As such, this phenomenon is inherently local, leading to important conceptual and practical consequences. First, this behavior can't be described within the framework of the standard DLVO theory, and specific extension (as in other extended-DLVO theories³⁻⁵) must be implemented if one wants to take this specific behavior into account. Second, this behavior can be exquisitely sensitive to kinetic processes such as NP surface ligand exchange, that could thus dynamically alter the propensity for NP aggregation over time³⁵. Third, our data could explain why selective aggregation and precipitation of like-charged nanoparticles (NPs) can be induced by monovalent cations at relatively low ion concentrations³⁶ unlike, for example, lipidic vesicles, where only very high concentrations of monovalent ions, unlike divalent ions, are required for aggregation³⁷. As the size of gold NPs in these experiments (as in our simulations) is much smaller than those of lipid vesicles, our data suggest that local nanoscopic interactions might be at the origin of such behavior.

Finally, we want to point out some limitations of our approach. First, the PMFs we computed are obtained from the separation of two NPs from an initial dimeric state. While this approach is helpful to discriminate between different NP-NP interfaces, there is no guarantee that our profiles represent the minimum free energy path for the opposite, and more frequent, process: nanoparticle aggregation. Rather, our profiles could be considered as upper limits for the aggregation process, that could instead have lower barriers and different minima. Also, computational approaches such as atomistic simulations inherently carry some systematic error, generally in the order of 1 kcal mol⁻¹ ³⁸. Second, it must be pointed out that a direct comparison of our data with experimental results can only be qualitatively for three main reasons. First, in our simulations we assume a single protonation state for all MUA ligands. This is not the case in experiments, and hence our total charge is much higher than that of a corresponding name-sake (*e.g.*, 33%OT) NP. Second, our simulations only consist of two NPs. As such, we are completely neglecting contributions arising from interactions between the NP dimer and other NPs, typically resulting, in experimental contexts, in larger NP assemblies. Third, inherent differences in ionic strength between experimental conditions and molecular simulations induce different electrostatic screening for NP dimerization. Of note, since the charge density in the MD simulations is likely higher than that in experimental conditions, the electrostatic barriers are likely underestimated in the MD simulations, potentially explaining why the barrier to transition from the ion-mediated minimum to the core-core minimum is relatively low in our *in-silico* modelling.

Taken together, our results suggest that electrostatic interactions taking place at the nanometer scale, in the form of charged ligand-ion-charged ligand complexes, promote attractive interactions between charged NPs. We anticipate that our results will remain valid not only for diverse NPs (*e.g.*, those carrying different charged ligands such as citrate), but that they will also be instrumental to explain phenomena taking place in biological systems. These could

include interactions between NPs and proteins, between NPs and lipid membranes (as in the accompanying manuscript (Lavagna et al.)) as well as direct protein-protein interactions such as those driving reversible protein aggregation or protein phase separation.

MATERIALS AND METHODS

Molecular Dynamics simulations. The systems investigated in this study consist of dimers of identical NPs in aqueous salt solution. For the NPs structures, we prepared models of mercapto undecane carboxylic acid (MUA) and octanethiol (OT) functionalized Au-NPs compatible with the OPLS forcefield³⁹ as derived by Salassi et al.⁴⁰ The core of the NP is composed of 144 Au atoms and 60 S atoms representing the grafting point of each ligand⁴¹. The icosahedral symmetry of the core was kept using an elastic network. The NP surface is protected by 60 ligands that are bound to the NP core via Au-S bonds. We generated various ligand shells with different OT-MUA ratio, which led to NPs with different total charge. The disposition of the grafted molecules is random for each OT-MUA ratio, unless described otherwise. Figure 5 shows the chemical structures of the OT and MUA ligands and a representative disposition of the grafted molecules.

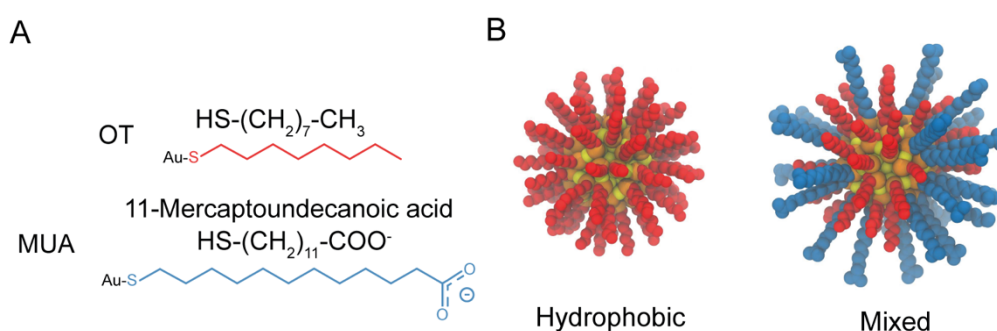


Figure 5: Structural and geometrical characteristics of NPs. A. The surfactants forming the ligands shell; B. NPs models for 100%OT and 50%OT.

For charged NPs, the system charge was neutralized adding sodium counterions. The TIP3P model was employed for water molecules. All the MD simulation were performed using the GROMACS 2018.3 package⁴². The van der Waals interactions were truncated using a cutoff value of 1.4 nm and a switching function was applied to the tail region (1.2 – 1.4 nm) to smoothly bring the van der Waals potential to zero at the cutoff distance. The bonds involving hydrogen atoms were constrained using the LINCS⁴³ and SETTLE algorithms⁴⁴. The integration time step was set to 2 fs.

For every system, we used umbrella sampling⁴⁵ to estimate the free energy profile (or potential of mean force, PMF) along the chosen reaction coordinate: the interparticle distance (ζ), which was defined as the distance between the center of mass of both NP cores. To generate starting configurations for every umbrella window, we pulled two NPs away from an initial dimer state to the complete separation. Dimer states were built by putting the NPs at distances short enough to spontaneously observe dimerization during the initial equilibration runs, which were performed using a Berendsen thermostat and a Berendsen barostat⁴⁶, with coupling time constants of 2 ps, to control the temperature (298 K) and pressure (1 atm). Then, NPs were pulled with a force of 1300 kJ mol⁻¹ nm⁻² and at constant velocity (0.001 nm ps⁻¹) while using a Nosé-Hoover chain thermostat⁴⁷ and a Parrinello-Rahman barostat⁴⁸, respectively, with coupling time constants of 1 ps to control the temperature (298 K) and pressure (1 atm). From this trajectory, we extracted configurations at equispaced values (every 0.2 nm) along the reaction coordinate ζ . Each configuration was equilibrated, using the same algorithms and parameters described above for the equilibration of the dimer states, while constraining its interparticle distance at the original value. Subsequently, a 60 ns production run (using the same algorithms and parameters employed for the pulling simulation) was carried out for every window. Then, we used the weighted histogram analysis method (WHAM) to reconstruct the free energy profile along the selected reaction coordinate, through the combination of the

umbrella histograms obtained for each of the windows, and to quantify the statistical errors on the estimated PMF⁴⁹. According to the analysis, the collected sampling per window was enough to maintain the statistical errors below ~ 1 kcal mol⁻¹.

Complexes. To investigate the formation of R-COO⁻: Na⁺: ⁻COO-R complexes as a function of the ionic strength and NP type, we calculated the total number of these interactions. We characterized the formation of these complexes by the presence of a sodium ion within a cutoff distance of 0.35 nm of two or more carboxylate groups simultaneously. To do so, we first computed the distances between all R-COO⁻: Na⁺ pairs and subsequently defined an event (complex formation) for every sodium ion that was able to bridge (showing distances below the mentioned 0.35 nm threshold⁵⁰ or more carboxylates from different NPs. For each complex, we also computed the number of ligands involved in every event.

Ligand density maps. To investigate the interaction between NPs as a function of the interparticle distance, we calculated, as a 2-D density map, the spatial distribution of the beads forming both the hydrophobic and hydrophilic ligands. Considering the cylindrical geometry of the dimers, these 2-D density maps were computed as a function of the distance along the axis passing through the center of mass of both NP cores and the radial distance from this axis. The density was normalized by the number of bins for a given radius. Moreover, in order to analyze the ligand distribution on the NP surface and how this influences the aggregation energy profile, we also generated maps of the ligand densities in the ligand shell. To do so, we projected the cartesian coordinates of selected beads (see below) onto the plane that contains the center of mass of one of the NP cores and is perpendicular to the line that joins the center of mass of both NP cores. This allowed us to describe the position of the selected beads (the terminal carbon bead of every ligand) in a 2-D map using longitude and latitude coordinates. Following this approach, the projections of the center of mass of both NP cores coincide and

define the origin of the map (i.e., they have both coordinates [0, 0]), and the ligand density distribution can be easily described using the above-mentioned selected beads for both MUA and OT ligands as reference. These quantities were computed by averaging over the MD trajectories.

Charge density. To evaluate the distribution of charges around NPs, we computed the charge density. To do so, we binned the simulation box in sub-volumes and assigned the number of positive and negative charges per sub-volume ($q_e \text{ nm}^{-3}$). Subsequently, we projected the charges per bin onto the xy plane of the simulation box ($q_e \text{ nm}^{-2}$).

Synthesis and characterization of gold nanoparticles. Synthesis of gold nanoparticles functionalized with a binary mixture of thiolated molecules was done in two major steps: synthesis of oleylamine coated gold nanoparticles and then ligand exchange of oleylamine by a desired mixture of thiols.

1. Synthesis of oleylamine-coated gold nanoparticles (OAm-AuNPs): All chemicals were purchased from Sigma-Aldrich and used without further purification. 392 mg of hydrogen tetrachloroaurate trihydrate ($\text{HAuCl}_4 \cdot 3\text{H}_2\text{O}$) were dissolved in 32 mL of oleylamine and 40 mL of n-octane, in a three-necks round bottom flask and stirred at room temperature under argon atmosphere. The solution of reducing agent was prepared by dissolving 170 mg of tert-butylamine-borane complex (tBAB) in 8 mL of oleylamine and injected to the flask containing the gold solution. The reaction was stirred from one to two hours before quenching it with 120 mL of ethanol. The so-obtained nanoparticles were purified by cycles of centrifugation, with washing in ethanol and redispersion in dichloromethane. The final purified particles were dried under vacuum.

2. Ligand exchange of OAm-AuNPs. To make MUA:OT gold nanoparticles, the solution containing the two thiolate ligands was prepared by dissolving 30 mg of mercaptoundecanoic acid (MUA) and 24 μ L of n-octanethiol (OT) (feed ratio of 1 to 1) in 30 mL of dichloromethane. 60 mg of nanoparticles were dissolved in 4 mL of dichloromethane and the solutions were mixed and stirred for two days. The nanoparticles were then washed 5 times with a mixture of acetone and dichloromethane by centrifugation and purified with DI-water using 30kDa Amicon Ultra-15 centrifugal filter devices. Finally, the concentrated nanoparticles were lyophilized. MUS:OT was prepared by the same protocol as was reported previously. Conventional transmission electron microscopy (TEM) was used to obtain particle size distribution on a carbon film coated grid containing dry powder. Image segmentation and size analysis were carried out in ImageJ (NIH, ver. 1.53c). Feret's diameters were used as the NP diameter.

Nuclear magnetic resonance (NMR) spectroscopy was utilized for characterizing particle purity and for obtaining ligand ratios. To do cryogenic electron tomography, a dispersion at concentration of 40 mg/ml was prepared for MUS:OT gold nanoparticles, and for MUA:OT nanoparticles at 20 mg/ml. The freshly prepared dispersions were used for this method.

Cryogenic electron tomography of nanoparticle dispersions. A 4 μ L aliquot of dispersion of gold nanoparticles was placed on a quantifoil grid (1.2/1.3, EMS) and then a filter paper was applied to remove excess dispersion. The thin film of dispersion was vitrified by liquid ethane in a homemade plunge freeze device. The vitrified grid was loaded to a cryogenic holder Gatan 626 (Gatan, USA) and transferred to a transmission electron microscope F20 (ThermoFisher, USA). Images were recorded in low dose mode at magnification of 50000X at 4096 X 4096 pixels. Tilt series were acquired from -60° to 60° at an incremental angle of 2° by Tomography 4.0 (ThermoFisher, USA). The tilt series images were binned by 2 and then aligned by Inspect3D

(Thermofisher, USA). The reconstruction was carried out in Inspect3D (Thermofisher, USA) using SIRT algorithm, at the final pixel size of 0.41nm. The identification of locations of nanoparticles in the tomograms was carried out in Imaris (Oxford Instruments, UK) and the 3D centroid positions were exported to calculate radial distribution functions.

ASSOCIATED CONTENT

Supporting Information. The file Petretto_SI_NPaggregation.docx is available free of charge.

AUTHOR INFORMATION

Corresponding Author

*Stefano Vanni stefano.vanni@unifr.ch

AUTHOR CONTRIBUTIONS

EP, SV and FS conceptualized and designed the research; EP performed the MD simulations and data analyses with the help of PC; QKO performed the cryo-ET experiment; FO and MT synthesized and characterized the NPs used for the cryo-ET experiments; SV supervised the project; the manuscript was written through contributions of all authors.

ACKNOWLEDGMENTS

SV and EP acknowledge support by the Swiss National Science Foundation through the National Center of Competence in Research Bio-Inspired Materials. PC acknowledges support from the Novartis Foundation for Biomedical Research grant #17C139. FS, FO, TM, and QO

thank the Swiss National Science Foundation for financial support (grant number 200020_185062). This work was supported by grants from the Swiss National Supercomputing Centre (CSCS) under project ID s1011 and s1030. All authors thank Giulia Rossi, Enrico Lavagna, and Davide Bochicchio for many fruitful discussions, for sharing their results and for a critical reading of the manuscript.

REFERENCES

- (1) Hiemenz, P. C.; Rajagopalan, R.; Rajagopalan, R. *Principles of Colloid and Surface Chemistry, Revised and Expanded*; CRC Press, 2016. <https://doi.org/10.1201/9781315274287>.
- (2) Misra, R. P.; Das, S.; Mitra, S. K. Electric Double Layer Force between Charged Surfaces: Effect of Solvent Polarization. *Journal of Chemical Physics* **2013**, *138* (11). <https://doi.org/10.1063/1.4794784>.
- (3) Sin, J. S. Influence of Solvent Polarization and Non-Uniform Ion Size on Electrostatic Properties between Charged Surfaces in an Electrolyte Solution. *Journal of Chemical Physics* **2017**, *147* (21). <https://doi.org/10.1063/1.5002607>.
- (4) Pashley, R. M.; McGuiggan, / P M; Ninham, / B W; Brady, J.; Evans, D. F. *Direct Measurements of Surface Forces between Bilayers of Double-Chained Quaternary Ammonium Acetate and Bromide Surfactants*; 1986; Vol. 90.
- (5) Butt, H. J.; Cappella, B.; Kappl, M. Force Measurements with the Atomic Force Microscope: Technique, Interpretation and Applications. *Surface Science Reports*. Elsevier 2005, pp 1–152. <https://doi.org/10.1016/j.surfrep.2005.08.003>.

(6) Merk, V.; Rehbock, C.; Becker, F.; Hagemann, U.; Nienhaus, H.; Barcikowski, S. In Situ Non-DLVO Stabilization of Surfactant-Free, Plasmonic Gold Nanoparticles: Effect of Hofmeister's Anions. *Langmuir* **2014**, *30* (15), 4213–4222. <https://doi.org/10.1021/la404556a>.

(7) Reginald Thio, B. J.; Lee, J. H.; Meredith, J. C.; Keller, A. A. Measuring the Influence of Solution Chemistry on the Adhesion of Au Nanoparticles to Mica Using Colloid Probe Atomic Force Microscopy. *Langmuir* **2010**, *26* (17), 13995–14003. <https://doi.org/10.1021/la1020516>.

(8) Grasso, D.; Subramaniam, K.; Butkus, M.; Strevett, K.; Bergendahl, J. A Review of Non-DLVO Interactions in Environmental Colloidal Systems. *Reviews in Environmental Science and Biotechnology* **2002**, *1* (1), 17–38. <https://doi.org/10.1023/A:1015146710500>.

(9) Vericat, C.; Vela, M. E.; Benitez, G.; Carro, P.; Salvarezza, R. C. Self-Assembled Monolayers of Thiols and Dithiols on Gold: New Challenges for a Well-Known System. *Chemical Society Reviews*. 2010, pp 1805–1834. <https://doi.org/10.1039/b907301a>.

(10) Pengo, P.; Şologan, M.; Pasquato, L.; Guida, F.; Pacor, S.; Tossi, A.; Stellacci, F.; Marson, D.; Boccardo, S.; Pricl, S.; Posocco, P. Gold Nanoparticles with Patterned Surface Monolayers for Nanomedicine: Current Perspectives. *European Biophysics Journal*. Springer Verlag December 1, 2017, pp 749–771. <https://doi.org/10.1007/s00249-017-1250-6>.

(11) Pezzato, C.; Maiti, S.; Chen, J. L. Y.; Cazzolaro, A.; Gobbo, C.; Prins, L. J. Monolayer Protected Gold Nanoparticles with Metal-Ion Binding Sites:

Functional Systems for Chemosensing Applications. *Chemical Communications*. Royal Society of Chemistry June 21, 2015, pp 9922–9931. <https://doi.org/10.1039/c5cc00814j>.

(12) Pieters, G.; Prins, L. J. Catalytic Self-Assembled Monolayers on Gold Nanoparticles. *New Journal of Chemistry*. Royal Society of Chemistry September 16, 2012, pp 1931–1939. <https://doi.org/10.1039/c2nj40424a>.

(13) Dubois, L. H.; Nuzzo, R. G. *Synthesis, Structure, and Properties of Model Organic Surfaces*; 1992; Vol. 43.

(14) Woodruff, D. P. The Interface Structure of N-Alkylthiolate Self-Assembled Monolayers on Coinage Metal Surfaces. *Physical Chemistry Chemical Physics*. 2008, pp 7211–7221. <https://doi.org/10.1039/b813948b>.

(15) Häkkinen, H. The Gold-Sulfur Interface at the Nanoscale. *Nature Chemistry*. June 2012, pp 443–455. <https://doi.org/10.1038/nchem.1352>.

(16) Liu, X.; Yu, M.; Kim, H.; Mameli, M.; Stellacci, F. Determination of Monolayer-Protected Gold Nanoparticle Ligand-Shell Morphology Using NMR. *Nature Communications* **2012**, 3 (1), 1–9. <https://doi.org/10.1038/ncomms2155>.

(17) Xu, X.; Rosi, N. L.; Wang, Y.; Huo, F.; Mirkin, C. A. Asymmetric Functionalization of Gold Nanoparticles with Oligonucleotides. *Journal of the American Chemical Society* **2006**, 128 (29), 9286–9287. <https://doi.org/10.1021/ja061980b>.

(18) Manson, J.; Kumar, D.; Meenan, B. J.; Dixon, D. Polyethylene Glycol Functionalized Gold Nanoparticles: The Influence of Capping Density on

Stability in Various Media. *Gold Bulletin* **2011**, *44* (2), 99–105.
<https://doi.org/10.1007/s13404-011-0015-8>.

(19) Daniel, M.-C.; Astruc, D. Gold Nanoparticles: Assembly, Supramolecular Chemistry, Quantum-Size-Related Properties, and Applications toward Biology, Catalysis, and Nanotechnology. **2004**.
<https://doi.org/10.1021/cr030698>.

(20) Moglianetti, M.; Ponomarev, E.; Szybowski, M.; Stellacci, F.; Reguera, J. Co-Precipitation of Oppositely Charged Nanoparticles: The Case of Mixed Ligand Nanoparticles. *Journal of Physics D: Applied Physics* **2015**, *48* (43), 434001. <https://doi.org/10.1088/0022-3727/48/43/434001>.

(21) Jonassen, H.; Kjørniksen, A. L.; Hiorth, M. Effects of Ionic Strength on the Size and Compactness of Chitosan Nanoparticles. *Colloid and Polymer Science* **2012**, *290* (10), 919–929. <https://doi.org/10.1007/s00396-012-2604-3>.

(22) Centrone, A.; Penzo, E.; Sharma, M.; Myerson, J. W.; Jackson, A. M.; Marzari, N.; Stellacci, F. The Role of Nanostructure in the Wetting Behavior of Mixed-Monolayer- Protected Metal Nanoparticles. *Proceedings of the National Academy of Sciences of the United States of America* **2008**, *105* (29), 9886–9891. <https://doi.org/10.1073/pnas.0803929105>.

(23) Ong, Q.; Luo, Z.; Stellacci, F. Characterization of Ligand Shell for Mixed-Ligand Coated Gold Nanoparticles. *Accounts of Chemical Research* **2017**, *50* (8), 1911–1919. <https://doi.org/10.1021/acs.accounts.7b00165>.

(24) Cardellini, A.; Alberghini, M.; Govind Rajan, A.; Misra, R. P.; Blankschtein, D.; Asinari, P. Multi-Scale Approach for Modeling Stability,

Aggregation, and Network Formation of Nanoparticles Suspended in Aqueous Solutions. *Nanoscale* **2019**, *11* (9), 3925–3932. <https://doi.org/10.1039/c8nr08782b>.

(25) Munaò, G.; Correa, A.; Pizzirusso, A.; Milano, G. On the Calculation of the Potential of Mean Force between Atomistic Nanoparticles. *European Physical Journal E* **2018**, *41* (3). <https://doi.org/10.1140/epje/i2018-11646-3>.

(26) Zhang, X.; Zhang, J. S.; Shi, Y. Z.; Zhu, X. L.; Tan, Z. J. Potential of Mean Force between Like-Charged Nanoparticles: Many-Body Effect. *Scientific Reports* **2016**, *6*. <https://doi.org/10.1038/srep23434>.

(27) Waltmann, C.; Horst, N.; Travesset, A. Potential of Mean Force for Two Nanocrystals: Core Geometry and Size, Hydrocarbon Unsaturation, and Universality with Respect to the Force Field. *Journal of Chemical Physics* **2018**, *149* (3). <https://doi.org/10.1063/1.5039495>.

(28) Sridhar, D. B.; Gupta, R.; Rai, B. Effect of Surface Coverage and Chemistry on Self-Assembly of Monolayer Protected Gold Nanoparticles: A Molecular Dynamics Simulation Study. *Physical Chemistry Chemical Physics* **2018**, *20* (40), 25883–25891. <https://doi.org/10.1039/c8cp04044c>.

(29) van Lehn, R. C.; Alexander-Katz, A. Ligand-Mediated Short-Range Attraction Drives Aggregation of Charged Monolayer-Protected Gold Nanoparticles. *Langmuir* **2013**, *29* (28), 8788–8798. <https://doi.org/10.1021/la400756z>.

(30) Sánchez-Iglesias, A.; Grzelczak, M.; Altantzis, T.; Goris, B.; Pérez-Juste, J.; Bals, S.; van Tendeloo, G.; Donaldson, S. H.; Chmelka, B. F.;

Israelachvili, J. N.; Liz-Marzán, L. M. Hydrophobic Interactions Modulate Self-Assembly of Nanoparticles. *ACS Nano* **2012**, *6* (12), 11059–11065. <https://doi.org/10.1021/nn3047605>.

(31) Nakanishi, H.; Deák, A.; Hólló, G.; Lagzi, I. Existence of a Precipitation Threshold in the Electrostatic Precipitation of Oppositely Charged Nanoparticles. *Angewandte Chemie International Edition* **2018**, *57* (49), 16062–16066. <https://doi.org/10.1002/anie.201809779>.

(32) Ong Q.; Mao T.; Anaraki N. I.; Richter Ł.; Malinverni C.; Xu X.; Olgiate F.; Henrique P.; Silva J.; Murello A.; Neels A.; Demurtas D.; Shimizu S.; Stellacci F. Cryogenic Electron Tomography to Determine Thermodynamic Quantities for Nanoparticle Dispersions.

(33) Verma, A.; Stellacci, F. Effect of Surface Properties on Nanoparticle-Cell Interactions. *Small*. January 4, 2010, pp 12–21. <https://doi.org/10.1002/sml.200901158>.

(34) Francia, V.; Montizaan, D.; Salvati, A. Interactions at the Cell Membrane and Pathways of Internalization of Nano-Sized Materials for Nanomedicine. *Beilstein Journal of Nanotechnology* **2020**, *11*, 338–353. <https://doi.org/10.3762/bjnano.11.25>.

(35) Dewi, M. R.; Laufersky, G.; Nann, T. A Highly Efficient Ligand Exchange Reaction on Gold Nanoparticles: Preserving Their Size, Shape and Colloidal Stability. *RSC Advances* **2014**, *4* (64), 34217–34220. <https://doi.org/10.1039/c4ra05035e>.

(36) Wang, D.; Tejerina, B.; Lagzi, I.; Kowalczyk, B.; Grzybowski, B. A. Bridging Interactions and Selective Nanoparticle Aggregation Mediated by Monovalent Cations. *ACS Nano* **2011**, *5* (1), 530–536. <https://doi.org/10.1021/nn1025252>.

(37) Ohki, S.; Düzgüneş, N.; Leonards, K. Phospholipid Vesicle Aggregation: Effect of Monovalent and Divalent Ions. *Biochemistry* **1982**, *21* (9), 2127–2133. <https://doi.org/10.1021/bi00538a022>.

(38) Wan, S.; Sinclair, R. C.; Coveney, P. v. Uncertainty Quantification in Classical Molecular Dynamics. *Philosophical Transactions of the Royal Society A: Mathematical, Physical and Engineering Sciences*. Royal Society Publishing May 17, 2021. <https://doi.org/10.1098/rsta.2020.0082>.

(39) Beveridge, D. L.; Jorgensen, W. L.) *For Reviews, See: (A) Levitt, M;* UTC, 1988; Vol. 110.

(40) Salassi, S.; Simonelli, F.; Bochicchio, D.; Ferrando, R.; Rossi, G. Au Nanoparticles in Lipid Bilayers: A Comparison between Atomistic and Coarse-Grained Models. *Journal of Physical Chemistry C* **2017**, *121* (20), 10927–10935. <https://doi.org/10.1021/acs.jpcc.6b12148>.

(41) Lopez-Acevedo, O.; Akola, J.; Whetten, R. Structure and Bonding in the Ubiquitous Icosahedral Metallic Gold Cluster Au₁₄₄ (SR) 60. *The Journal of* **2009**, *113*, 5035–5038. <https://doi.org/10.1021/jp8115098>.

(42) Abraham, M. J.; Murtola, T.; Schulz, R.; Páll, S.; Smith, J. C.; Hess, B.; Lindah, E. Gromacs: High Performance Molecular Simulations through Multi-

Level Parallelism from Laptops to Supercomputers. *SoftwareX* **2015**, 1–2, 19–25.
<https://doi.org/10.1016/j.softx.2015.06.001>.

(43) Hess, B.; Bekker, H.; Berendsen, H. J. C.; Fraaije, J. G. E. M. LINCS: A Linear Constraint Solver for Molecular Simulations. *Journal of Computational Chemistry* **1997**, 18 (12), 1463–1472. [https://doi.org/10.1002/\(SICI\)1096-987X\(199709\)18:12<1463::AID-JCC4>3.0.CO;2-H](https://doi.org/10.1002/(SICI)1096-987X(199709)18:12<1463::AID-JCC4>3.0.CO;2-H).

(44) Miyamoto, S.; Kollman, P. A. Settle: An Analytical Version of the SHAKE and RATTLE Algorithm for Rigid Water Models. *Journal of Computational Chemistry* **1992**, 13 (8), 952–962.
<https://doi.org/10.1002/jcc.540130805>.

(45) Torrie, G. M.; Valleau, J. P. Nonphysical Sampling Distributions in Monte Carlo Free-Energy Estimation: Umbrella Sampling. *Journal of Computational Physics* **1977**, 23 (2), 187–199. [https://doi.org/10.1016/0021-9991\(77\)90121-8](https://doi.org/10.1016/0021-9991(77)90121-8).

(46) Berendsen, H. J. C.; Postma, J. P. M.; van Gunsteren, W. F.; Dinola, A.; Haak, J. R. Molecular Dynamics with Coupling to an External Bath. *The Journal of Chemical Physics* **1984**, 81 (8), 3684–3690. <https://doi.org/10.1063/1.448118>.

(47) Evans, D. J.; Holian, B. L. The Nose-Hoover Thermostat. *The Journal of Chemical Physics* **1985**, 83 (8), 4069–4074. <https://doi.org/10.1063/1.449071>.

(48) Parrinello, M.; Rahman, A. Polymorphic Transitions in Single Crystals: A New Molecular Dynamics Method. *Journal of Applied Physics* **1981**, 52 (12), 7182–7190. <https://doi.org/10.1063/1.328693>.

- (49) Grossfield, A. WHAM: The Weighted Histogram Analysis Method. http://membrane.urmc.rochester.edu/wordpress/?page_id=126.
- (50) Heikkilä, E.; Martinez-Seara, H.; Gurtovenko, A. A.; Vattulainen, I.; Akola, J. Atomistic Simulations of Anionic Au₁₄₄(SR)₆₀nanoparticles Interacting with Asymmetric Model Lipid Membranes. *Biochimica et Biophysica Acta - Biomembranes* **2014**. <https://doi.org/10.1016/j.bbamem.2014.07.027>.